Experimental Outdoor Activity on Sonic Boom Assessment of the STRATOFLY MR3 Scale Model

Giovanni Fasulo [1], Sébastien Hengy [2], Bastien Martinez [2], Luigi Federico [1], Luciano De Vivo [1], Marie Albisser [2] and Andreas Zeiner [2]

Abstract

Despite the limited success of the Concorde, the last two decades have seen a resurgence of interest in commercial supersonic flight. In this context, the European Commission has funded the MOREandLESS project, under the Horizon 2020 plan, to assess the potential of some innovative high-speed aircraft configurations and to identify and mature the technologies needed to overcome the main obstacles to their deployment. In particular, the massive thunder-like noise produced when an aircraft breaks through the sound barrier represents one of the most persistent challenges of the supersonic regime. For this reason, a great deal of effort is devoted to the construction of various demonstrators to investigate the effects of different aircraft features on the sonic boom intensity. Through collaboration between ISL and CIRA, a series of outdoor investigation activities are and will be undertaken to provide a large amount of high-quality experimental data suitable for both sonic boom characterization and validation/refinement of current or novel analytical techniques for sonic boom estimation. The first test campaign, consisting of five free-flight tests, was carried out at the ISL (Saint-Louis, France) firing range (on 4th and 5th October 2022) on a reduced and slightly modified version of the STRATOFLY MR3 vehicle, launched with a 91 mm powder cannon at an initial Mach number of 4.7. To measure the sonic boom, ISL and CIRA deployed various types of sensors in the field. The gathered data were then post-processed to provide a sonic boom directivity diagram of the model and a comparison with the Whitham's modified linear theory predictions.

Keywords: *Sonic boom; MOREandLESS; STRATOFLY MR3; hypersonic aircraft; Whitham's modified linear theory.*

Nomenclature

A – Cross-sectional area
A_{eq} – Equivalent total area due to both volume and lift
A_l – Area due to lift
ATLLAS – Aero-Thermodynamic Loads on Lightweight Advanced Structures II
A_v – Area due to volume
CFD – Computation Fluid Dynamic
CIRA – Centro Italiano Ricerche Aerospaziali
CPA – Closest Point of Approach
ENU – East North Up
F – F-function
FFT – Fast Fourier Transform
HEXAFLY – High-Speed Experimental Fly Vehicles

HEXAFLY-INT – High-Speed Experimental Fly Vehicles-International
HIKARI – HIgh speed Key technologies for future Air transport
ISL – Institut franco-allemand de recherches de Saint-Louis
LAPCAT – Long-Term Advanced Propulsion Concepts and Technologies
RTK-GPS – Real Time Kinematic Global Positioning System
S – Aircraft planform area
STRATOFLY – Stratospheric Flying Opportunities for High-Speed Propulsion Concepts
W – Aircraft weight
a – Speed of sound

[1] *Italian Aerospace Research Centre, Capua, 81043, Italy, G.fasulo@cira.it*
[2] *Institut franco-allemand de recherches de Saint-Louis, Saint-Louis, 68300, France, Sebastien.HENGY@isl.eu*

b – Local span of aircraft planform at a given value of y-coordinate
l – Lifting pressures
q – Dynamic pressure
r – Perpendicular distance from trajectory to probes
x – Trajectory axis
y – Distance along the body axis
α – Flight-path angle
β – Prandtl-Glauert coefficient
γ – Ratio of specific heats
γ_d – Correction factor duration
γ_p – Correction factor pressure
θ – Mach angle

ξ – Dummy variable of integration
φ – Roll angle
ϕ – Propagation azimuth angle
F_n – Component of force normal to the free stream
M_∞ – Mach number
p_∞ – Reference pressure for a uniform atmosphere
p_v – Atmospheric pressure at aircraft altitude
y_0 – y value for which $\int F(y)\,dy$ is a maximum
Δp – N-wave peak pressure
Δt – N-wave duration
Δp_{adj} – Adjusted N-wave peak pressure
Δt_{adj} – Adjusted N-wave peak duration

1. Introduction

Although there are currently no supersonic civil aircraft in operation, significant research efforts are underway to develop new vehicles capable of revolutionizing the current concept of business and tourist air travel, especially in terms of reducing flight times and increasing the number of long-haul routes [1,2]. However, unlike Concorde, the design phase of new aircraft brings with it new challenges that were not as important at the time [3-6]. These include ensuring economic viability, environmental sustainability and human acceptance. In this context, the European Commission, under the Horizon 2020 Program and the natural follow-up to a series of European projects (ATLLAS I/II [7], LAPCAT I/II [8], HIKARI [9], HEXAFLY [10], HEXAFLY Int. [11], STRATOFLY [12]), has funded the MOREandLESS project [13] to assess the potential of some innovative high-speed aircraft configurations and to identify and mature the technologies needed to overcome the main obstacles to their deployment. The STRATOFLY MR3 (Fig 1) represents the main concept of this framework, namely a highly integrated system capable of flying long-distance routes, reaching Mach 5 in the cruise phase at an altitude of 30-35 km, and carrying many more passengers than the historic Concorde.

Fig 1. STRATOFLY MR3 aircraft

An important driver for the resurgence of civil supersonic aircraft lies in the potential for sonic boom reduction. In detail, when an aircraft goes supersonic, it moves through the air at speeds exceeding the local speed of sound (pressure propagation speed), which prevents pressure transmission of forces to the air regions ahead the plane, and all the disturbance wave fronts will coalesce to form a system of shock waves attached to the body itself [14]. These shock waves are generated continuously as long as the vehicle is supersonic and moves behind it in a cone-like shape. When it passes the observers, a sudden thunder-like noise, known as a sonic boom, hits them. The annoyance is so great that the government has banned civilian supersonic flight over land and restricted it to military aircraft (in designated areas only). This peculiar noise can indeed cause distress to humans and animals and even damage nearby structures. In particular, experience [15-17] shows that sonic booms, like other high-pitched sounds, can induce effects such as startle, sleep disturbance, and annoyance.

Since recent research has demonstrated that sonic booms can be reduced to publicly acceptable levels by careful modeling of the vehicle geometry (needle nose, slender fuselage, and delta or highly inclined wings) [18], the MOREandLESS project aims to explore and assess the potential of various innovative configurations. The sonic boom measurement procedure to characterize such vehicles consists of outdoor experimental activities on scale models launched from a cannon at very high speed. Specifically, a series of microphone sensors deployed on the test ground are set up to record the overpressure signature. The valuable information gathered during this research period and the subsequent post-processing analyses will be crucial to:

- provide experimental data to characterize the sonic boom of the aircraft configurations proposed in MOREandLESS;

- provide experimental data that will be useful for studying sonic boom characteristics at high Mach numbers;

- provide the necessary experimental data required to verify and refine analytical current/novel sonic-boom estimation techniques;

- provide a large, high quality experimental database suitable for both CFD tool development and validation.

The first test campaign envisaged by the project was carried out at the ISL proving ground located about 25 km far from the north of Saint-Louis (on 4th and 5th October, 2022), on a reduced and slightly modified version of the STRATOFLY MR3 vehicle. The size of the model was also a key factor in the choice of launch system, which led to the selection of a 91mm smooth-bore cannon. In detail, five free-flight tests were carried out, over a firing distance of 210 m, for initial Mach numbers of 4.7, for different projectile initial positions and for a zero initial angles of attack. In addition, to provide a comprehensive and efficient characterization of sonic boom across the entire roll angle range, three microdrones equipped with microphones and data recorders were flown stationary, vertically to the flight path, at an altitude of 10 to 50 meters.

In this work, Whitham's modified linear theory [19-21] is applied to determine the sonic boom characteristics of the launched MR3 model using the same input flight conditions as recorded for the experimental cases. The predicted overpressure signatures are then compared to the experimental results. Finally, the experimental data are adjusted to fully characterize the combined effects of roll motion and the model's non-axial symmetry on signature duration and peak pressure.

2. Test Ground, Projectile and Equipment

During a two-day field test on 4 and 5 October 2022, five shots were performed using a 91 mm smooth-bore cannon with the aim of measuring the sonic boom generated by hypersonic models at various roll angles. To achieve this, a revised variant of the STRATOFLY MR3 vehicle was developed compared to its original configuration. Indeed, in order to ensure that the projectile would reach the firing range target with fairly controlled dynamics, the model was not only downsized, but also slightly modified in its geometry. In addition, the careful design of a sabot package, consisting of four petals to fit around the projectile and keep it aligned in the center of the barrel, and of a pusher plate to prevent gas leakage, enabled this model to be fired with a smooth-bore gun properly.

To record sonic booms, ISL and CIRA deployed several microphones on the ground and in the air. In detail, the deployment protocol for each test was as follows:

- preparation of the test, including cannon setup, equipment inspection and microphones calibration;

- initialization of the ground equipment (microphones, cameras, radars);

- aerial deployment of the three stationary drones (each equipped with a microphone);

- integration of the free-flight model with its own sabot and installation in the cannon;

- start data recording;

- execution of the test;

- stop data recording;

- roll angle measurement frames recuperation.

The following subsections provide more details on the test ground, models, equipment, and procedures.

2.1. Fire Line and Gun Platform Description

The facility allows free-flight tests over firing distances up to 1000 m with rifled- or smooth-bore powder guns, for calibers from 12.7 mm to 105 mm. Projectile speeds ranging from Mach 0.6 up to 6.0 can be achieved, depending on the desired flow conditions as well as on the studied architectures. A photograph of the proving ground, including the retained measurement techniques, is shown in the following Fig 2.
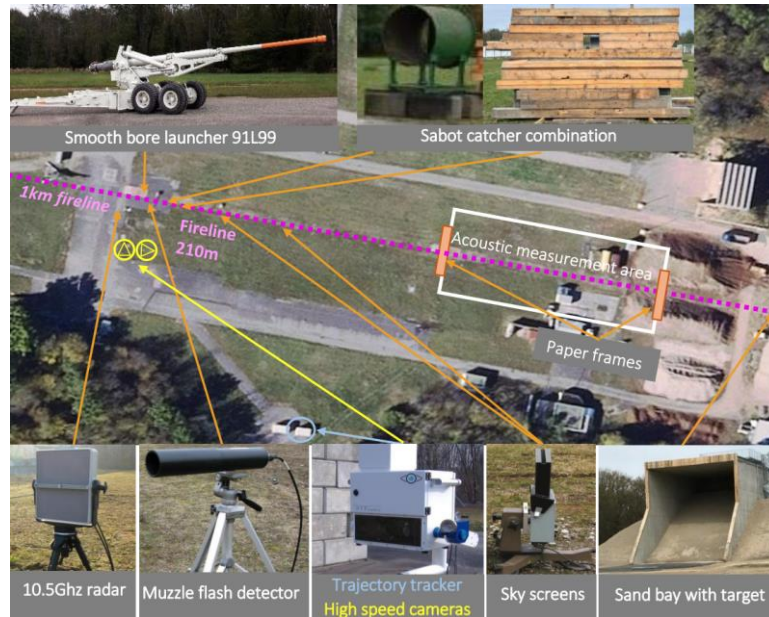

Fig 2. ISL proving ground and measuring techniques

The models were launched from a 91 mm smooth-bore powder gun under atmospheric conditions, over a distance of 210 meters on average and with rectilinear trajectories, with known initial Mach numbers, angles of attack and roll angles. Following the gun launch, the sabot petals separate from the projectile at a certain distance determined by the initial velocity and the total mass to be fired. Therefore, the models can be considered as free-flying from a minimum distance - of almost 10 meters in the present cases - where no perturbations from the gun or from the sabot occur anymore. A continuous Doppler radar (frequency of 10.52 GHz) located next to the launcher was used to determine the evolution of the projectile velocity along the trajectory and the associated total drag. The radar data are reduced and post-processed by means of a Fast Fourier Transform analyzer (FFT). Secondly, a 3D high-speed optical system developed by *Specialized Imaging Ltd*. was deployed to record videos of the projectiles in flight. This system consists of a trajectory tracker located on the side of the firing line. The tracker is equipped with a high-speed camera and a motorized mirror ensuring the follow-up of the projectile in flight. These complementary measurement techniques provide additional output signals which could yield to the determination of the 3D positions along the trajectory, especially the roll position. However, in the present experiments, two paper frames were deployed at the entrance and the exit of the acoustic measurement zone in order to evaluate the roll position at both stations. Furthermore, two sky screens were deployed along the fire-line for correcting the motorized mirror scanning speeds of the trajectory tracker, in order to ensure a correct follow-up of the projectiles in flight. Finally, the triggering of the experiments is ensured thanks to a muzzle flash detector.

2.2. Projectile and Sabot Design

The present study involved the design and manufacture of a modified sub-scale model of the STRATOFLY MR3 configuration. Specifically, the model was designed to be sub-scaled and launched

from a 91 mm smooth-bore powder gun at the ISL proving ground. In addition, since the MR3 shape (Fig 3a) produces a constant lifting effect, it was also necessary to perform a geometrical modifications to make them suitable for firing range tests, otherwise the vehicles would not reach the firing range target. As it can be seen in the following Fig 3b, the proposed modifications were performed on the lee-side shape of each geometry since the wind-side part of each geometry is responsible for wave generation and propagation to the ground. Thus, in order to avoid asymmetric lifting effects during the free-flight tests and to maintain the bottom contour, symmetry was introduced. The latter was obtained by mirroring the lower part to the top, resulting in no lift generation at zero angle of attack. Finally, the canards and the fins were neglected for simplicity. As such, the sonic boom investigated in the scheduled experiments should be representative of the ones associated to the real configurations.
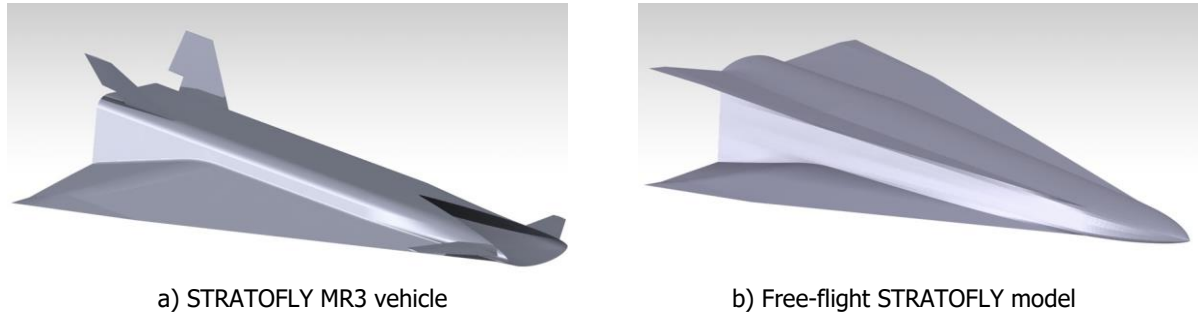

a) STRATOFLY MR3 vehicle   b) Free-flight STRATOFLY model

Fig 3. Proposed geometry modifications for the free-flight tests

The modified STRATOFLY MR3 version was numerically and experimentally investigated by means of Computational Fluid Dynamic simulations (CFD), wind-tunnel and shock-tunnel tests. Experimental results consist of free-flying motions, inside both wind- and shock-tunnels, which were recorded by means of a high-speed camera. The main aerodynamic coefficients were determined using an image processing code developed at ISL, based on images extracted from the acquired videos. These investigations were first conducted to check the stability of the modified geometry, for both 0° and 90° of roll positions. As a result, the final modified geometry resulted in a mass of 501.7 g and a length of 203 mm, with the center of gravity longitudinally located 132.6 mm far from the nose.

Additionally, a sabot package was designed to successfully launch the modified STRATOFLY MR3 model. The resulting sabot package and projectile, shown in the following Fig 4, has a total mass of 1 kilogram and consists of four petals produced on a *Markforged Mark II* filament printer and an aluminum pusher plate.
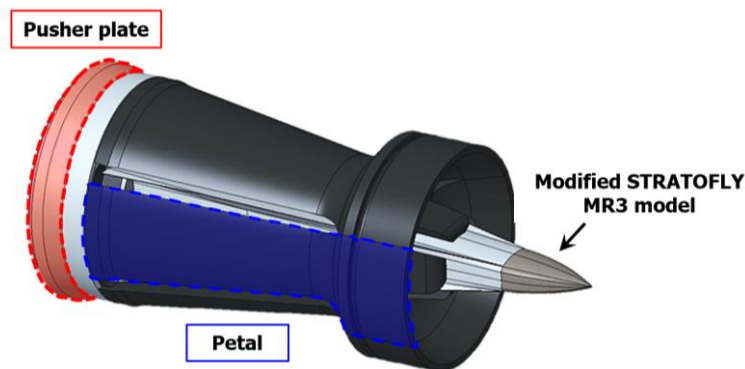

Fig 4. Sabot package and the modified STRATOFLY MR3 model designed for the free-flight tests

The latter was required to prevent gas leakage and to ensure a proper transmission of the pressure forces to the mechanical structure of both the projectile and the sabots during the gun launch.

2.3. Acoustic Equipment

The measurement setup deployed by ISL consisted of acoustic sensors allowing the acquisition of the overpressure signatures in different frequency bands (from the low frequencies to the classical acoustic frequencies). The measurements were undertaken at various points down the range with 1/4-inch

Bruel&Kjaer microphones of type 4938. Specifically, fifteen microphones were deployed on the ground, at a 30 centimeters height, at five different CPA (Closest Point of Approach) distances of 5, 10, 15, 20 and 30 meters on three lines at distances of 70, 85 and 100 meters from the 90 mm canon muzzle (Mic1 to Mic15 of Fig 5). On the other hand, CIRA extended the measurement setup adding four 1/4-inch *PCB* pressure field prepolarized 377A12 microphones (Ch1 to Ch4 of Fig 5), at a height of one meter and at distances of approximately 5 and 10 meters from the trajectory.
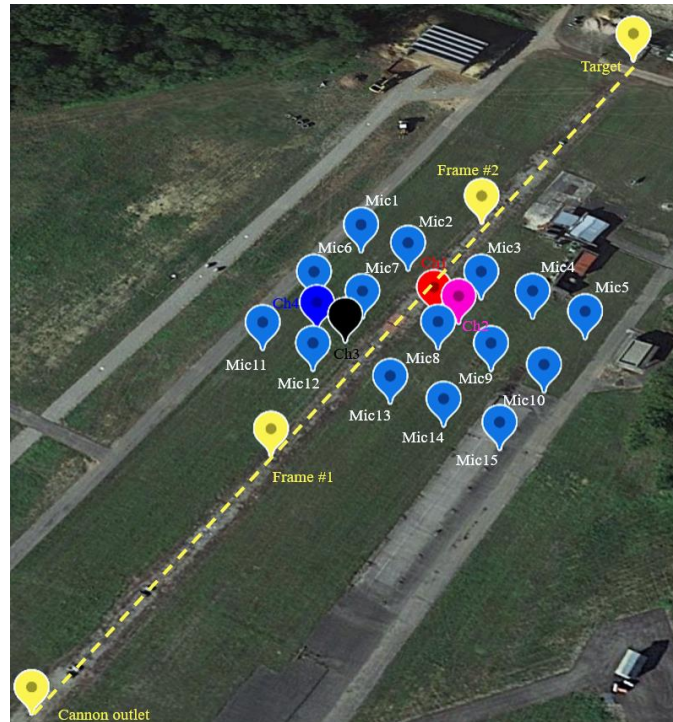

Fig 5. Position of ISL and CIRA ground microphones, roll angle detection frames, cannon outlet and target

Table 1 provides detailed information on the location of the acoustic sensors. The coordinates are given in an East North Up (ENU) reference frame with the cannon outlet used as the origin.

Table 1. Positions of ground microphones

Label	East [m]	North [m]	Up [m]
Mic1	4.6	104.9	-1.8
Mic2	14.4	103.0	-1.8
Mic3	29.1	100.1	-1.5
Mic4	38.9	98.4	-1.5
Mic5	48.8	96.5	-1.5
Mic6	45.9	81.8	-1.5
Mic7	36.3	83.6	-1.6
Mic8	26.3	85.5	-1.6
Mic9	11.6	88.2	-1.6
Mic10	1.8	90.0	-1.8
Mic11	-1.2	75.2	-1.8
Mic12	8.7	73.5	-1.6

Mic13	23.4	70.7	-1.4
Mic14	33.2	68.9	-1.4
Mic15	43.1	67.1	-1.4
Ch1	22.7	93.4	-0.6
Ch2	27.5	92.7	-0.6
Ch3	11.1	81.7	-0.7
Ch4	5.4	82.9	-0.8

In addition, to obtain a comprehensive and efficient characterization of sonic boom across the entire roll angle range, three drones were used. During each flight, they were set in stationary flight above the position of the microphones deployed on the field, perpendicularly to the shooting line, at heights varying from 10 to 50 m (depending on the drone and the test). Each drone was equipped with one RTK-GPS (Real Time Kinematic Global Positioning System) that allows for position estimation with a maximum error in the order of magnitude of 10 centimeters, at a 5 Hz sampling rate (refer to Table 2 to Table 4).

Table 2. Position of Phantom 3 "P3O3" during each shot

Test #	East [m]	North [m]	Up [m]
1	33.8	100.8	22.6
2	16.9	98.6	33.4
3	15.5	90.8	29.0
4	8.4	89.4	15.3
5	9.8	98.0	26.0

Table 3. Position of Phantom 4 "P4" during each shot

Test #	East [m]	North [m]	Up [m]
1	57.0	79.8	6.2
2	48.4	83.7	26.2
3	13.5	79.1	19.3
4	9.9	86.0	18.4
5	8.3	91.7	44.1

Table 4. Position of Phantom 3 "P3OASyS" during each shot

Test #	East [m]	North [m]	Up [m]
1	41.3	70.5	30.2
2	60.8	76.9	24.8
3	23.5	100.0	26.2
4	12.6	104.6	24.0
5	62.5	119.7	0.5

Each drone was also equipped with a data recorder of type *Roland R-07* and a *Sennheiser KE4-211-9* electret microphone, that allows for peak pressure measurements at values of more than 160 dB without distortion. The data recording was triggered manually, separately on each of the three drones. In order to synchronize the data issued from the drone measurements, a transient noise was generated at a distance of 2 meters away from the three drones gathered on the ground.

The three drones used for the measurements were of the same shape and size. They were two *DJI Phantom 3 Pro* and one *DJI Phantom 4 Pro*. The microphones associated with each drone will be referred to as P3O3, P3OASyS and P4 in the remainder of this paper.

For safety reasons, the drones had to be set in stationary flight (Fig 6) before the projectile could be moved from the storage facility and loaded into the cannon.

Fig 6. Three drones in stationary flight above the shooting line

The data acquisition for the ISL 15 microphones deployed on the field was handled with a data recorder from the *TEAC Corp.* operated by a Personal Computer (Fig 7) with a sampling frequency of 192 kHz. While, the data acquisition and storage for the CIRA microphones was handled with an 8-channel real-time sound level integrator and analyzer, from the *imc Corp.*, at a sampling rate of 51.2 kHz per channel.
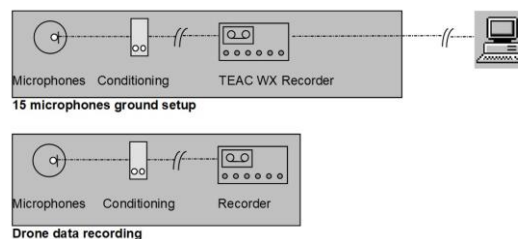

Fig 7. Data recording setup for both ground and drone sensors

Specifically, the beginning and the ending of the acquisition of the signals was performed manually during the countdown process of the recorded shot, and once the shot was triggered.

3. Data and Procedures for Post-Processing

The gathered data must be converted into a format that supports data analysis and provides a comprehensive understanding of the tests. This involves measuring parameters such as initial test conditions (speed, roll angle, angle of attack, etc.), environmental conditions (temperature, pressure, etc.), projectile speed profiles, and model roll angles for each of the five shots.

A brief description was provided in the following subsections.

3.1. Test Matrix

The test matrix, shown in Table 5, was created to track the various tests. It includes details of the model's initial speed, atmospheric pressure, temperature and humidity for each shot, which are essential for proper Mach number estimation.

Table 5. Overview of the test matrix

Test #	Initial speed [m/s]	Initial Mach [-]	Atmospheric Pressure [hPa]	Temperature [°C]	Humidity [%]
1	1616	4.7	995.4	19	69
2	1617	4.7	995.2	20	59
3	1605	4.7	995.7	14	89
4	1609	4.7	995.2	18	72
5	1612	4.7	994.9	23	51

Specifically, it comprises:

- three shots where the configurations have a vertical initial position (Fig 8a);
- two shots in which the configurations have a horizontal initial position (Fig 8b).

a) Vertical position   b) Horizontal position

Fig 8. Projectile initial positions (back view)

For illustrative purposes, examples of snapshots taken by the two high-speed cameras (used for sabot separation and impact assessment, respectively) are shown in Fig 9.
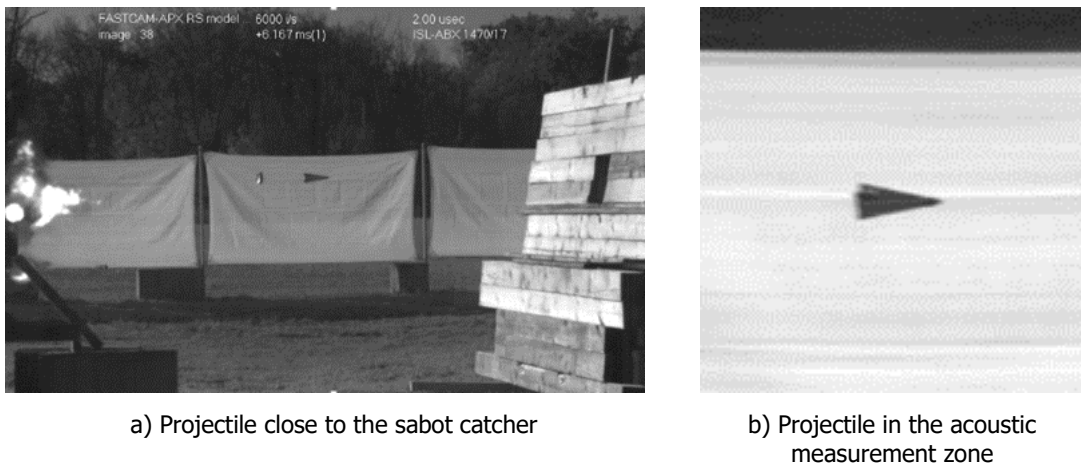

a) Projectile close to the sabot catcher   b) Projectile in the acoustic measurement zone

Fig 9. Snapshot of the projectile in flight

3.2. Roll Angles Estimation

The non-axisymmetric projectile produces a different sonic boom depending on which side of the model faces the microphones, resulting in a sound field that varies with the model's roll angle. Since an accurate evaluation of the roll angles associated with microphone recordings of sonic booms is quite complicated, a reasonable approximation has been introduced in the remainder of this paper. In

particular, the sound measured at position C' was considered related to the roll angle at the detach point B of the shock wave (Fig 10) generated by the supersonic model.
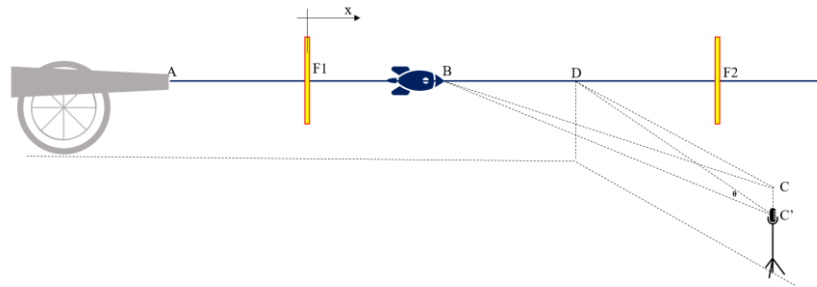

Fig 10. Representation of the positioning of roll angle detection targets (F_1 and F_2) and of the shock wave path considered for roll angle estimation ($\overline{BC'}$)

During each test, the roll motion was not imposed, but was a result of the manufacturing uncertainties of the model and the initial position, and to evaluate it, two paper frames were installed at the entrance and at the exit of the acoustic measurement zone (F_1 and F_2 in Fig 10). Specifically, Table 6 summarizes the roll angle measurement of each shot at both stations.

Table 6. Roll angle measurements for each test

Test #	Initial position	Roll angle frame 1 φ_1 [deg]	Roll angle frame 2 φ_2 [deg]	Direction of rotation
1	Vertical	0.5	18.6	Anticlockwise
2	Vertical	39.8	63.1	Anticlockwise
3	Vertical	122.0	141.8	Anticlockwise
4	Horizontal	-39.5	-50.6	Clockwise
5	Horizontal	9.5	3.5	Clockwise

As shown in Fig 11, all roll angles refer to the vertical upward direction; more precisely, the orange and red arrows denote the angle measured at the first and second frames (F_1 and F_2 in Fig 10), respectively.
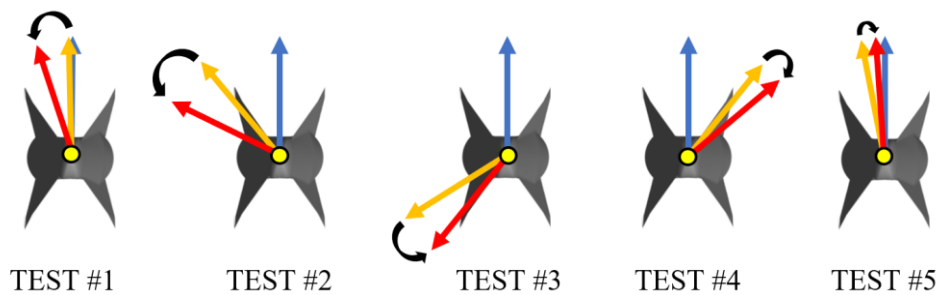

Fig 11. Sketch of roll angle measurements for each test

On the basis of these results, it was possible to determine the evolution of the roll angle as a function of range (or as a function of time) by assuming linear interpolation (assumption relevant due to the very slow roll rate). Therefore, considering a model characterized by a constant angular velocity within the measurement zone, the roll angle can be estimated as follows:

$$\varphi(x) = \frac{\varphi_2 - \varphi_1}{\overline{F_1 F_2}} x + \varphi_1 \tag{1}$$

G. Fasulo, S. Hengy, B. Martinez, L. Federico, L. De Vivo, M. Albisser, A. Zeiner

To estimate the effective roll angle for each test and microphone, the x coordinate was set equal to the difference between the distance $\overline{AB}$ and the distance from the cannon outlet to the first paper frame ($\overline{AF_1}$):

$$\overline{F_1B} = \overline{AB} - \overline{AF_1} \tag{2}$$

The value of $\overline{AB}$ can be calculated using the geometric acoustic model (refer to the following subsection), while the value of $\overline{AF_1}$ remains constant for each test and is equal to 52.4 m.

3.3. Geometric Acoustic Model

The shooting range geometry shown in Fig 12 consists of the cannon and several acoustic sensors deployed on the test ground. In each of the five tests performed, the model leaves the muzzle (point A) traveling at Mach 4.7 and proceeding towards point D. The shock wave system produced by the projectile moving through the air at supersonic speed expands outward behind the model at the speed of sound and along a direction ($\overline{BC'}$), depending on the Mach angle θ, i.e. the Mach number.
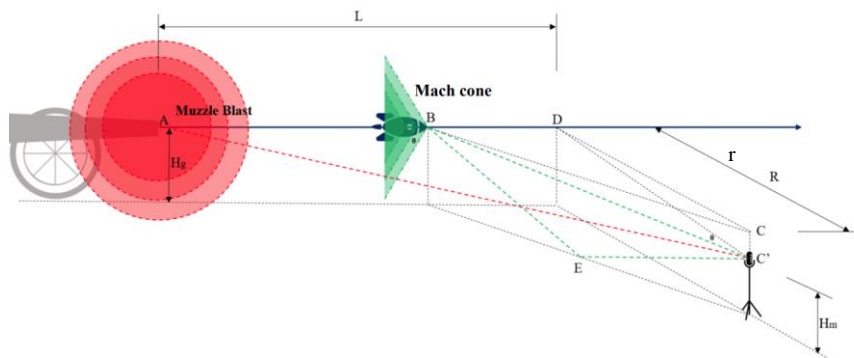

Fig 12. Geometric sketch of the test recording

Assuming constant projectile speed, the distance $\overline{AB}$ can simply be determined according to the following equation:

$$\overline{AB} = L - \sqrt{r^2 + \Delta H^2}\, tg(\vartheta) \tag{3}$$

In this equation, ϑ represents the Mach angle, L is the distance measured parallel to the trajectory from the probe to the cannon outlet, r is the ground projection of the perpendicular distance from the probe to the trajectory, and ΔH is the difference between the elevation of the gunshot trajectory and the height of the probe measured from the ground.

However, if the projectile speed is not constant, such as due to air drag, it is necessary to consider the projectile speed profile and thus compute $\overline{AB}$ by solving the system of equations between its definition (Eq. 3) and the Mach angle formula ($\vartheta(x) = asin(1/M(x))$, where $M(x)$ is a function of the distance. Substituting it into the $\overline{AB}$ definition, the following equation can be solved numerically:

$$\overline{AB} = L - \sqrt{r^2 + \Delta H^2}\, tg\left[asin\left(\frac{1}{M(\overline{AB})}\right)\right] \tag{4}$$

3.4. Roll Angle Adjustment and Estimation

Although the presented model considers the difference between the elevation of the gunshot trajectory and the height of the probes when modeling the sonic boom ray paths, a model roll angle adjustment needs to be introduced. Fig 13 clearly shows that a roll angle of zero degrees (measured from the default coordinate system, indicated by yellow) does not indicate a perfectly horizontal configuration with respect to the probes, but rather a slightly different one.
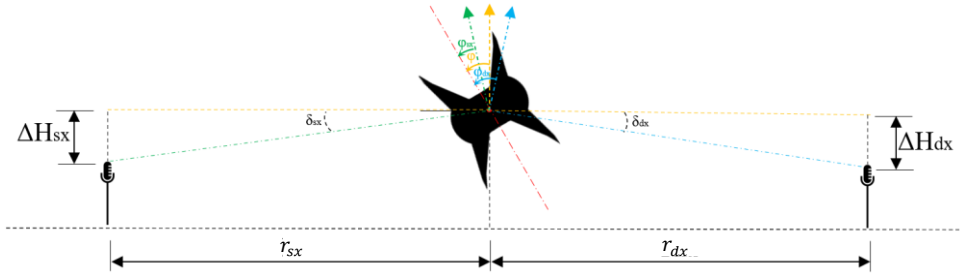
Fig 13. Front view of the first three test setup

Specifically, the correction of angles was carried out using two local coordinate systems. The aim was to set the roll angle to zero when the model is horizontally positioned (on-track) with respect to the acoustic sensor and equal to 90 degrees when the model is in a vertical configuration with respect to the probe. The new local coordinate systems were obtained by summing (blue coordinate system) or subtracting (green coordinate system) the angles between the horizontal line and the line that joins the fire trajectory to the probes, to the roll angle φ measured from the vertical upward direction. The decision to add or subtract was based on the relative position of the probes to the shot trajectory (according to Fig 13, left or right).

$$\varphi_{sx} = \varphi - \delta_{sx} = \varphi - tan^{-1}\left(\frac{\Delta H_{sx}}{r_{sx}}\right) \tag{5}$$

$$\varphi_{dx} = \varphi + \delta_{dx} = \varphi + tan^{-1}\left(\frac{\Delta H_{dx}}{r_{dx}}\right) \tag{6}$$

Additionally, the model's double symmetry, from an acoustic perspective, implies the existence of four distinct angular positions in which the projectile appears unchanged when rotated along its axis. This means that an external listener will perceive the same model's sonic booms (only direct shock) four times in a 360-degree rotation (see. Fig 14).
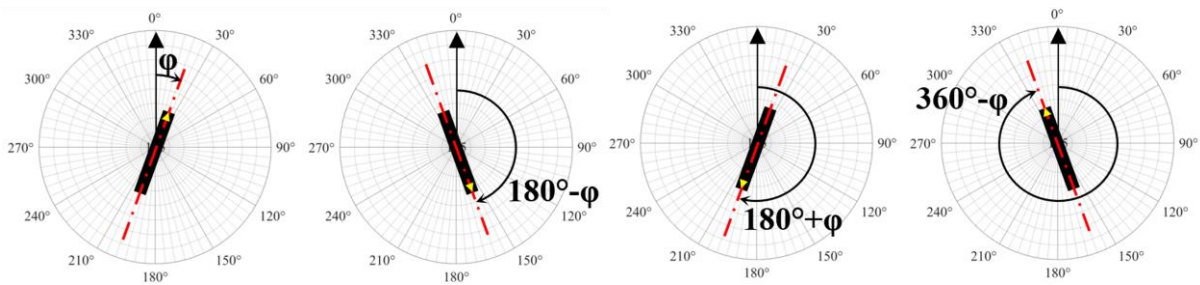

Fig 14. Equivalent configurations due to the model's double symmetry

Therefore, the model roll angles were reported in the range of 0-90° (Table 7), which were calculated for each microphone position in the field and for each shot.

Table 7. ISL and CIRA estimated roll angles for each shot and microphone [degrees]

Label	Test #1	Test #2	Test #3	Test #4	Test #5
Mic1	18.7	61.6	38.6	41.4	11.1
Mic2	30.2	73.3	27.1	30.7	21.9
Mic3	4.6	47.6	52.7	55.8	3.2
Mic4	8.3	51.2	49.0	51.2	1.2
Mic5	9.2	51.8	48.2	49.4	2.8
Mic6	14.7	56.6	42.9	39.0	12.4
Mic7	26.3	68.3	31.3	28.4	23.2
Mic8	0.8	42.6	56.9	53.4	1.9

Mic9	4.4	46.1	53.3	48.8	2.5
Mic10	5.3	46.9	52.4	47.0	4.1
Mic11	10.9	51.5	47.2	36.6	13.7
Mic12	22.4	63.3	35.6	26.0	24.5
Mic13	3.1	37.6	61.1	51.0	0.7
Mic14	0.5	41.2	57.5	46.4	3.8
Mic15	1.4	41.9	56.7	44.7	5.4
Ch1	5.2	47.7	52.3	52.6	0.5
Ch2	8.0	50.5	49.4	49.6	2.5
Ch3	17.6	59.1	40.1	34.6	16.6
Ch4	12.4	53.9	45.4	39.3	11.7
P3O3	61.4	15.2	64.6	70.8	32.3
P4	16.1	85.0	66.9	79.4	61.4
P3OASyS	47.5	73.2	18.2	72.5	1.4

3.5. Closest Point of Approach Estimation

To characterize the MR3 model sonic boom, the geometric relationship between the microphone sensors and the projectile must be computed for each shot. This also includes the estimation of the Closest Point of Approach (CPA), which is the minimum distance between the firing line (cannon exit and exit frame positions, i.e. the yellow line in Fig 14) and the acoustic sensors. The following Table 8 contains the distance of the CPA for ISL ground microphones (Mic1 to Mic15) and CIRA (Ch1 to Ch4).

Table 8. ISL and CIRA estimated CPA for each ground microphone

Label	CPA [m]
Mic1	14.7
Mic2	4.9
Mic3	10.4
Mic4	20.3
Mic5	30.3
Mic6	14.8
Mic7	5.0
Mic8	10.3
Mic9	20.4
Mic10	30.2
Mic11	15.0
Mic12	5.0
Mic13	10.2
Mic14	20.1
Mic15	30.1

Ch1	5.4
Ch2	10.1
Ch3	4.2
Ch4	9.9

The CPA distance for ground microphones remained constant for all shots. On the other hand, for the microphones mounted on drones P3O3, P4, and P3OASyS, the reference position for each drone was estimated by calculating the mean value of the data measured during stationary flight for each recording. Specifically, Table 9 reports the CPA distance for each test performed and drone:

Table 9. Estimated CPA [m] for drone-mounted microphones and for each shot

Label	Test #1	Test #2	Test #3	Test #4	Test #5
P3O3	27.2	33.7	29.3	29.1	38.1
P4	41.9	41.7	19.5	19.5	45.2
P3OASyS	41.2	52.1	26.9	25.2	39.6

4.   Analysis of Gunshot Recordings

To perform the tests, a conventional firearm was used, which employed a confined explosive charge to push the model out of the gun barrel. In this type of launching apparatus, the projectile plugs the bore before leaving the gun barrel, blocking the pressurized gases inside. Once the projectile exits, the high-pressure propellant gases are no longer confined in the barrel and flow from the muzzle at supersonic velocity, generating a shock discontinuity as it impacts and compresses the atmosphere [22]. The sound associated with such a shock wave is known as "muzzle blast". This phenomenon is directly related to the weapon's configuration, including the thermodynamic state of the muzzle flow and the geometry of the gun muzzle.

In addition, since the projectile moves through the air at speeds exceeding the local speed of sound, a system of shock waves attached to the body itself are produced [14]. Specifically, a body with simple geometry, such as axisymmetric projectiles, generally produces two shock waves: a bow shock wave, attached to the front of the body and a tail shock wave, attached to the rear part of the body. While, a body characterized by complicated geometry (i.e. aircraft), typically has a much larger number of shock waves, which, at very large distances (far-field), tend to coalesce into only two shock waves (N-wave signature), as in the case of simple geometry. In the far field, the bow shock of the N-wave signature corresponds to a rapid local compression of the air. This is followed by expansion to a value below atmospheric pressure, after which there is a sudden recompression at the tail shock. The sound associated with this sudden pressure change is called "sonic boom", precisely, N-wave presents two rapid pressure variation, so two booms occur. However, if the time interval between those two rapid compressions is small, the human ear is unable to distinguish between them and hears only one explosive sound. On the other hand, at larger time intervals (on the order of 0.07 seconds or more), the ear can distinguish two different booms. The sonic boom signature moves with the aircraft and is associated with continuous supersonic flight, not just with breaking the sound barrier. Therefore, as long as the aircraft is supersonic, the sonic boom is generated continuously.

Fig 15 presents an example of gunshot noise, recorded under carefully controlled conditions, by one of the deployed microphones. As can be seen, sonic booms and a muzzle blast characterize the time history of the sound pressure generated by the supersonic model launched with a cannon. Specifically, Fig 15a shows, in chronological order, the sonic booms of the model, the sonic booms associated with the shock waves of the sabot pusher plate (see Fig 9) and, finally, the muzzle blast. However, the purpose of the experimental tests was to characterize solely the acoustic component of the sonic boom generated by the MR3 model. For this reason, the sonic booms generated by the sabot pusher plate and the muzzle blast were excluded from the post-processing analyses. Specifically, when focusing on the projectile's sonic boom (see Fig 15b), two signals can still be clearly distinguished. Indeed, if solid

surfaces are nearby (the ground in the test case), the passing supersonic shock wave will be partially absorbed and reflected. As a result, the probe will detect both the direct and reflected booms, with a delay that depends on the path difference.
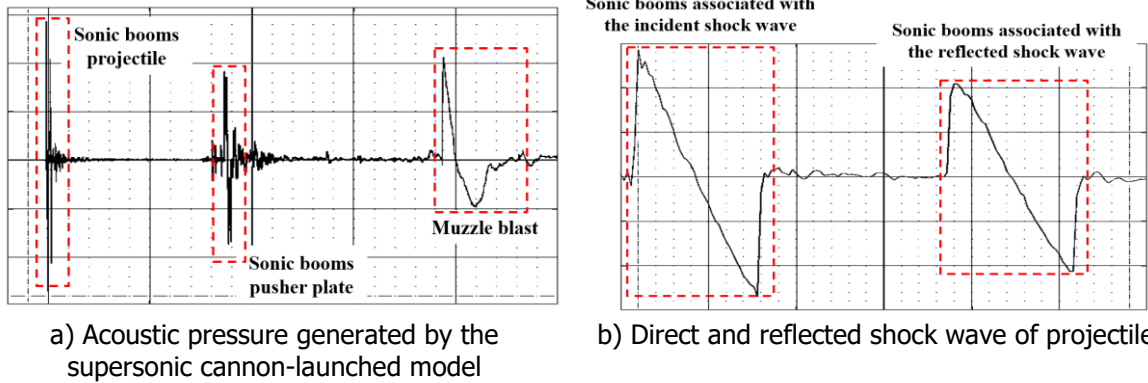

a) Acoustic pressure generated by the supersonic cannon-launched model

b) Direct and reflected shock wave of projectile

Fig 15. Time history of the acoustic pressure recorded during Test #5 from Ch1

Details of the field data from five different firing tests for the four CIRA microphone sensors are presented below. The acoustic overpressure signature time history (Fig 16) shows the arrival of the direct shock waves of the supersonic projectile at the microphone. The sequence of detections, Ch3 - Ch1 - Ch4 - Ch2, is consistent with the arrangement of the probes, for each of the five tests performed. Indeed, the delay between the signals is related to the varying time required for the shock waves to propagate at the speed of sound along different specific paths between the projectile and the probes.
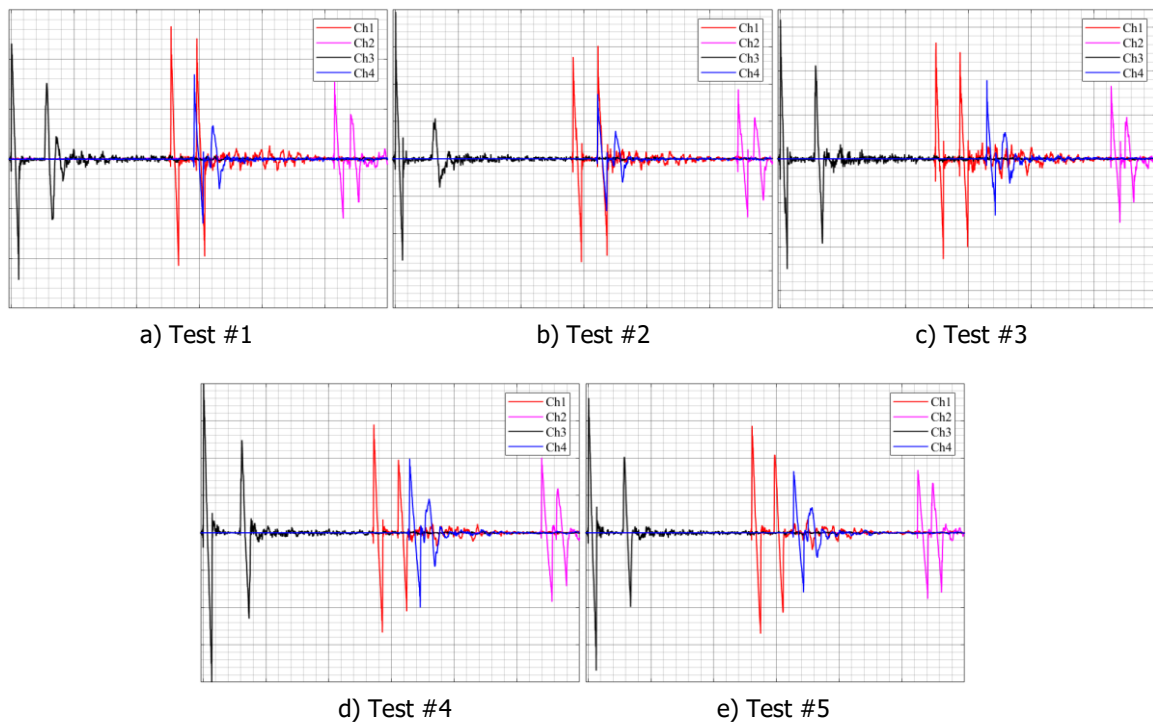

a) Test #1

b) Test #2

c) Test #3

d) Test #4

e) Test #5

Fig 16. Time-history of sonic boom sound pressures resulting from direct and reflected supersonic projectile shock waves, plotted chronologically and grouped for each test.

The subsequent significant event is the arrival of the reflection of the shock wave from the ground. Note that the reflection has a slightly smaller amplitude due to ground absorption and the longer propagation path through the air. In addition, although the relative distance between the trajectory and the probes is the same for each test, the time between two signals, recorded in different sessions, is usually not equal. This is due to differences in Mach number (i.e., different initial speed) and speed

of sound (i.e., different temperature conditions), which affect the time required for the shock wave to propagate.

Fig 17 provides a clearer representation of the time-history of the sonic booms measured by multiple microphones during one of the five tests. The graph shows the signals of four microphone sensors collected during test number five, thus resulting from the same projectile speed profile and sound speed value. To enable comparison of different overpressure signatures, a common starting point in time was established. Specifically, the time instant preceding the instantaneous rise in sound pressure caused by the bow shock wave.
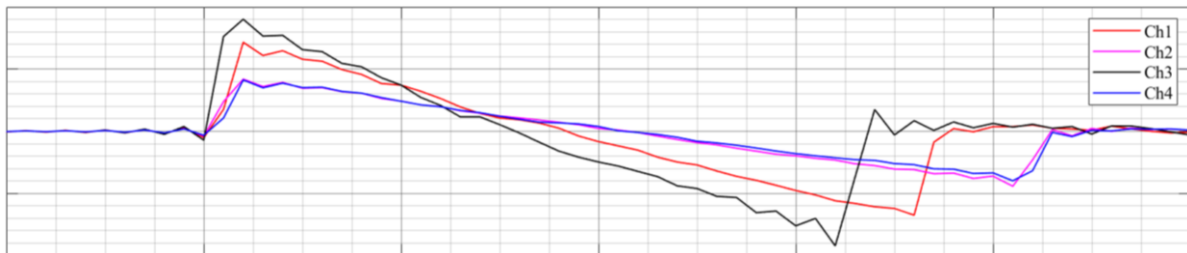
Fig 17. Time-history of sonic boom sound pressures resulting from direct supersonic projectile shock waves measured by four microphones during Test #5 and plotted using a common initial time

The variation in peak pressure and signature duration can be attributed to two primary factors: acoustic divergence and rotational motion of the projectile. According to the sonic boom theory, the acoustic pressure peak decreases with distance from the trajectory and simultaneously the distance (duration) between the leading and trailing N-waves increases. Therefore, the noise anisotropy resulting from the rotational motion of the projectile (and its non-axisymmetry) is hardly observable in such a plot (Fig 17). Nevertheless, the acoustic divergence effect can be precluded by plotting in a graph the signals recorded by the same microphone sensor during each test performed, as shown in Fig 18.
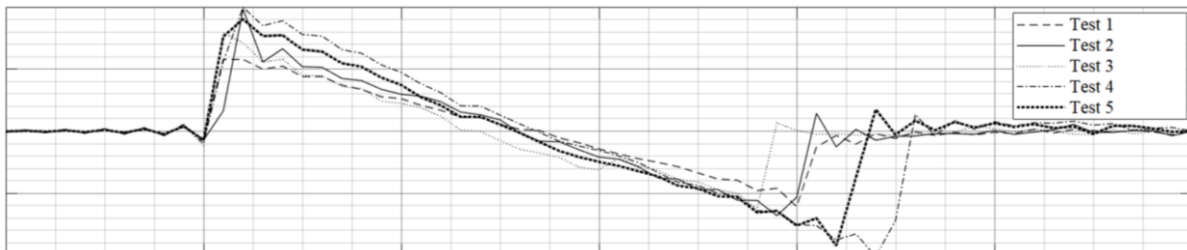

Fig 18. Time-history of sonic boom sound pressures resulting from direct supersonic projectile shock waves measured by the microphone Ch3 and plotted using a common initial time

Using a standard projectile in ammunition shape, the expected sonic boom signature should present a similar peak pressure and duration. However, it is clear from the figure that the peak pressure and duration of the N-wave vary significantly depending from shot to shot, particularly increasing significantly for shots number 4 and 5 (the first three shots were fired with the projectile set vertically in the cannon, while the fourth and fifth shots were fired with the projectile set horizontally). This confirms that the attitude (roll angle) of the projectile during the flight has an impact on the perceived shock wave at the measurement point.

4.1. Modified Whitham's Linear Theory Applied to the Modified MR3 Model

Whitham's theoretical studies [19,20] have provided a method for estimating the bow shock pressure rise from an axisymmetric supersonic projectile. Specifically, if the flow is steady, homogeneous, irrotational, inviscid, and supersonic and the body of revolution is sufficiently smooth with a pointed nose, the flow perturbations can be expressed as integrals, where the source distribution is the simple body area distribution:

$$F(y) = \frac{1}{2\pi} \int_0^y \frac{A''(\xi)}{\sqrt{y-\xi}} d\xi \tag{7}$$

where, $A(\xi)$ is the cross-sectional area of the body as a function of axial distance, ξ is a dummy variable of integration and y is a variable identifying a characteristic curve, and designated by a distance along the body axis.

According to Whitham's hypothesis, for a generic body that satisfies the above assumptions and considering a region sufficiently far away from the body (so that the signature evolves into the classical N-wave), Whitham's asymptotic relations can be used:

$$\Delta p = \frac{2^{1\backslash 4}\,\gamma\,p_\infty\,(M_\infty^2-1)^{1\backslash 8}}{(\gamma+1)^{1\backslash 2}}\sqrt{\int_0^{y_0} F(y)\,dy}\;\; r^{-3\backslash 4} \tag{8}$$

$$\Delta t = 2\,\frac{2^{1\backslash 4}\,(\gamma+1)^{1\backslash 2}M_\infty}{a(M_\infty^2-1)^{3\backslash 8}}\sqrt{\int_0^{y_0} F(y)\,dy}\;\; r^{1\backslash 4} \tag{9}$$

where:

- γ is the ratio of specific heats (1.4 for air);
- a is the speed of sound;
- p_∞ is the reference pressure for a uniform atmosphere;
- M_∞ is the flow Mach number;
- y_0 is the y value for which $\int F(y)\,dy$ is a maximum;
- r is the minimum distance from model to probe;

The original concept was limited to axisymmetric objects only. However, Whitham and Walkden [21] later extended this theory to non-axisymmetric and lifting bodies, taking into account an equivalent total area resulting from both volume and lift.

$$A_{eq}(y,\phi) = A_V(y,\phi) + A_L(y,\phi) \tag{10}$$

The area contribution due to volume (Fig 19) should be estimated from the normal projection of the area intercepted by the Mach cutting planes (supersonic area rule). While, to calculate the area due to lift is first necessary to solve for the intercept of the Mach cutting planes and the wing camber surface and then integrate the lifting pressures $l(x,y,\phi)$ along such line to determine the component of force $F_n(y,\phi)$ normal to the free stream, in the y position and in the ϕ direction. Finally, the area distribution is determined by applying this force as follows:

$$A_L(y,\phi) = \frac{\beta}{2q}\int_0^y F_n(\xi,\phi)d\xi \tag{11}$$

where β is the Prandtl-Glauert coefficient of compressibility and q is the dynamic pressure.
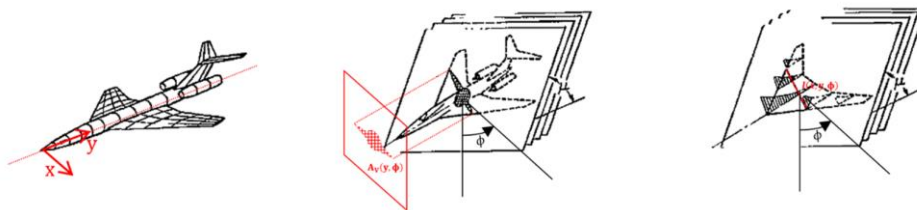

Fig 19. Illustration of the equivalent area calculation procedure

It is important to note that the supersonic area rule may not be accurately defined at higher Mach numbers, particularly for slender but not quite sharp bodies, and during steady climbs [23]. Therefore, a normal area distribution, typically used for axi-symmetric bodies and blunt shapes, was utilized to compute the F-function. Specifically, the area due to volume (Fig 20a) was estimated using the CATIA V5 CAD software by measuring the area of the section resulting from the intersection of a plane perpendicular to the model's longitudinal axis and the model itself. The process was repeated for the 200 points where the model was sliced. On the other hand, the estimation of the equivalent area component due to lift requires more modelling effort and more sophisticated input data to derive, such as the lifting pressures. For this reason, a reasonably accurate approximation was considered [24]:

$$A_L(y, \phi) = \frac{\beta \, W \cos(\alpha) \cos(\phi)}{1.4 \, p_v \, M_\infty^2 \, S} \int_0^y b(y) \, dy \qquad (12)$$

where, $b(y)$ is the local span of aircraft planform at a given value of y-coordinate, W is the aircraft weight, α is the flight-path angle, ϕ is the ray-path azimuth angle, p_v is the atmospheric pressure at aircraft altitude and S is the aircraft planform area. In the most critical situation, when α and ϕ are zero, the formula becomes a function of only the y-coordinate:

$$A_L(y) = \frac{\beta \, W}{1.4 \, p_v \, M_\infty^2 \, S} \int_0^y b(y) \, dy \qquad (13)$$

The modified STRATOFLY MR3 model has a weight of 4.9 N, atmospheric pressure is approximately 100 kPa, M_∞ is 4.7, and S is around 0.0040 m^2 (one wing). Specifically, considering the contribution of lift associated with the four wings, the area distribution due to lift (as shown in Fig 20b) results much smaller than the area due to volume.
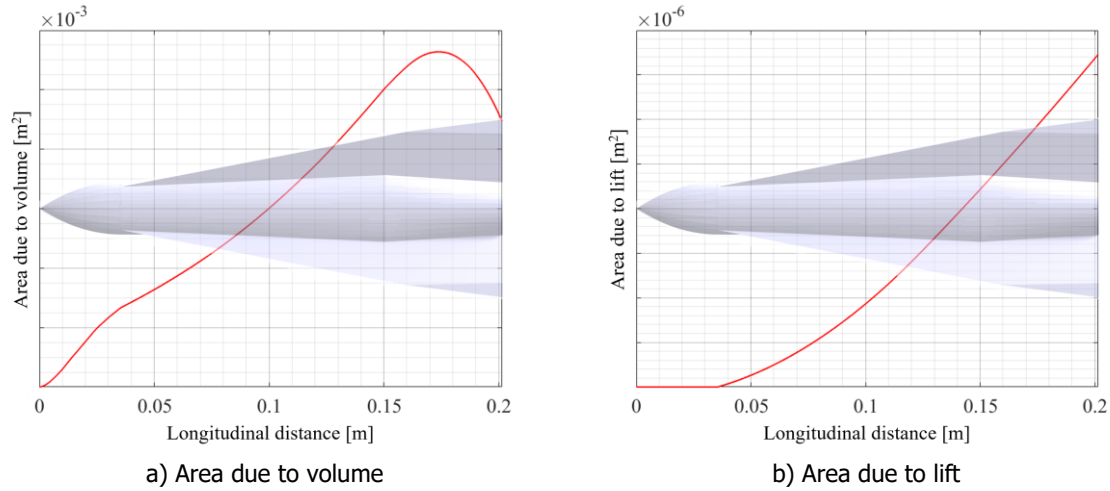

a) Area due to volume   b) Area due to lift

Fig 20. Modified STRATOFLY MR3 model area distribution

Therefore, we can confidently neglect the area due to lift and calculate Whitham's F-function (Fig 21) using Eq. 7.
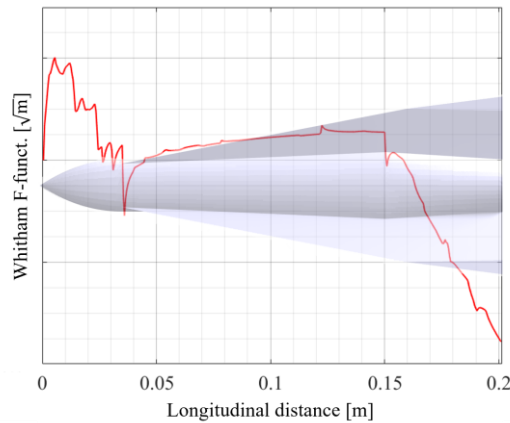

Fig 21. Modified STRATOFLY MR3 Whitham's F-function

Since different atmospheric pressure and speed of sound conditions occurred between each test (Table 5), mean values were considered, and Eqs. 8 and 9 were then used to predict the characteristics of the N-waves.

Fig 22a and Fig 22b present both the predicted and measured N-waves in terms of peak pressure level and duration as a function of the distance from the shot trajectory (CPA). The scatter plots show the measured values, while the line shows the predicted behavior as defined by the Whitham theory.
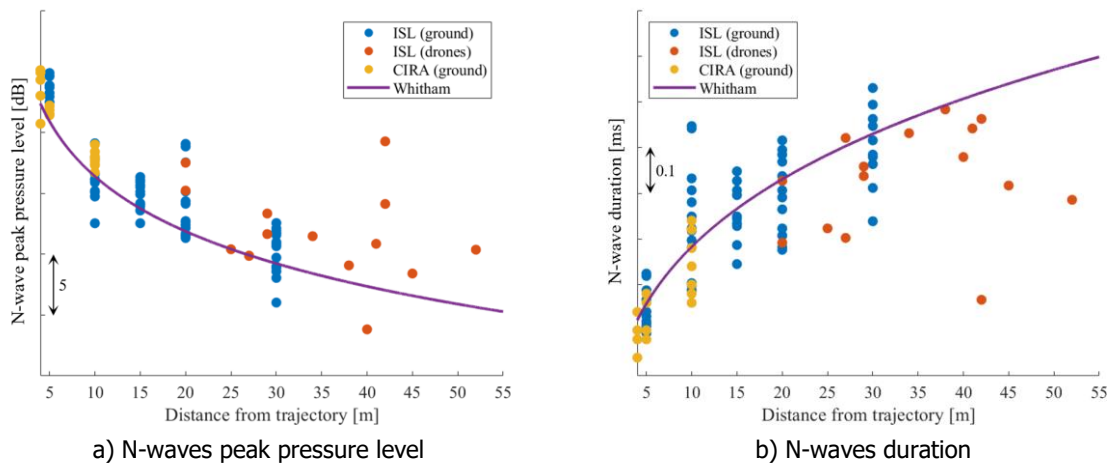
a) N-waves peak pressure level   b) N-waves duration

Fig 22. Comparison of experimental and theoretical N-wave properties as a function of CPA distances

One of the purposes of applying the above procedure was to determine whether neglecting certain assumptions underlying the theory affected the results for the investigated configuration. Indeed, Whitham's approach accurately predicts the sonic boom of a supersonic aircraft, at least in the far field region. However, in the hypersonic regime, the neglected nonlinear effects in Whitham's formulation become dominant, rendering it generally inapplicable [25]. Furthermore, the use of normal area distribution instead of the supersonic area rule does not enable accurate estimation of shock waves or description of the model's noise directivity. Nevertheless, even at high Mach numbers (4.7 in this case), and despite the normal area distribution, the correlation between experiments (mean observed N-wave duration and the peak pressure) and theory for the modified STRATOFLY MR3 scale model appears to be quite good (Fig 23). This is in agreement with NASA experimental studies on sonic boom phenomena [26], which showed very good agreement with the flow field for complex aircraft model configurations and high Mach numbers in the lower lift range.

The definition of mean behavior was crucial, as the wide dispersion of signature characteristics measured cannot be fully explained by the employed theoretical approach. Indeed, the observed fluctuations at fixed CPA distances (thus, excluding the divergence phenomena) were mainly caused by the non-axial symmetry and rolling motion of the model, which are not considered in the theoretical description. Specifically, its evaluation was based on the multiple measurements obtained with ground microphones at CPA distances of 5, 10, 15, 20, and 30 meters (Fig 23).
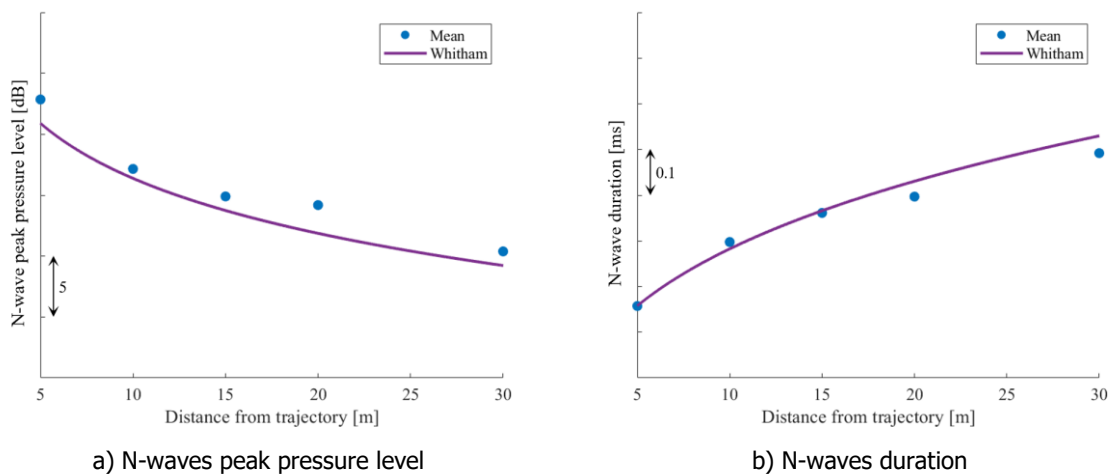

a) N-waves peak pressure level   b) N-waves duration

Fig 23. Observed mean N-waves (blue circles) compared to theoretical N-waves (purple solid line)

The peak pressure level estimation presents a mean absolute error of 1.5 dB and a standard deviation of 0.6 dB. The mean error and standard deviation for N-wave duration estimation are 0.018 ms and 0.017 ms, respectively.

4.2. Modified MR3 Model Sonic Boom Directivity

The final section of this paper focuses on the noise directivity characteristics of the model and their impact on the duration and pressure peak of the N-waves. To accomplish this, the roll angle was calculated for each shot and microphone deployed in the field (refer to Table 6 Table 7). Furthermore, since the CPA distance affects the N-wave signatures, it was necessary to adjust the measured values for an accurate comparison. For that purpose, correction factors for each CPA distance were calculated from the average values measured for CPA distances between 5 and 30 m (Table 10 shows the correction factors). This allows the projection of the measurements performed at any CPA distance ($\Delta p_{(CPA)}$ and $\Delta t_{(CPA)}$), to a common 5 meters CPA measurement position ($\Delta p_{adj(5)}$ and $\Delta t_{adj(5)}$).

$$\Delta p_{adj(5)} = \Delta p_{(CPA)} \, \gamma_{p(CPA)} \tag{14}$$

$$\Delta t_{adj(5)} = \Delta t_{(CPA)} \, \gamma_{t(CPA)} \tag{15}$$

Table 10. Correction factor [-] for various CPA distances based on average values (pressure levels and durations) measured for CPA distances between 5 and 30 meters

Correction factor	CPA=5m	CPA=10m	CPA=15m	CPA=20m	CPA=30m
$\gamma_{p(CPA)}$	1.00	1.03	1.05	1.06	1.08
$\gamma_{t(CPA)}$	1.00	0.84	0.76	0.71	0.64

A total of 110 different roll angle observations obtained from 19 ground microphones and 3 microphones on stationary drones were analyzed. Specifically, the Fig 24a and Fig 24b show the adjusted values (at 5m CPA distance) for the duration and the peak pressure of the N-waves, respectively, and as a function of roll angle. The results are reported in the 0-90° range as the projectile is twice symmetrical (Fig 14).
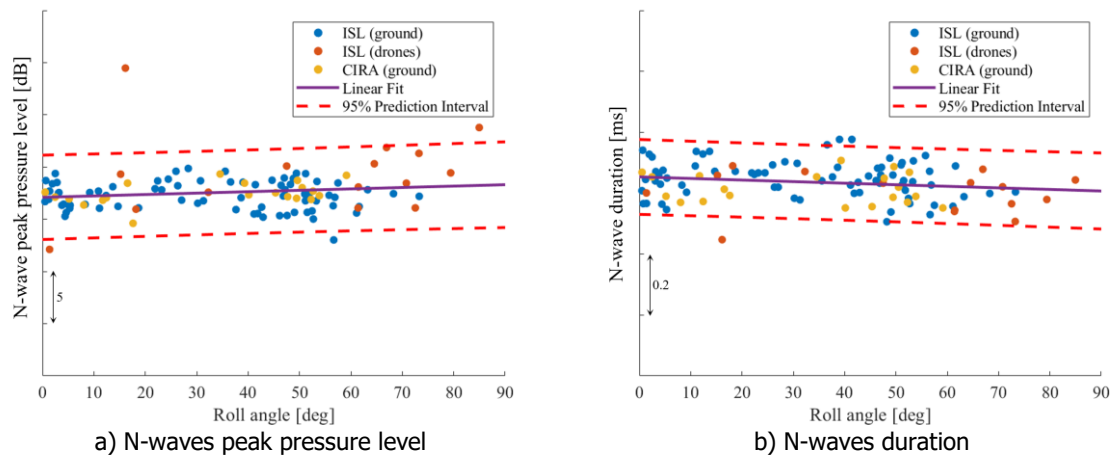

a) N-waves peak pressure level

b) N-waves duration

Fig 24. Corrected (for 5 meters CPA distance) N-waves for each of the 110 different roll angle observations obtained from the 19 ground microphones and the three drone microphones

The pressure of booms produced by the model in flight exhibits a slight increasing trend with roll angle, while the time duration of the N-waves appears to decrease with roll angle. Nevertheless, according to the ground microphone data, the maximum and minimum values for both duration and peak pressure are not observed at the lowest and highest roll angles and vice versa, but rather at roll angles between approximately 30 and 60 degrees.

Examining the results grouped by test (Fig 25), the N-wave peak pressure levels measured for Test #4 revealed a larger deviation from the expected trend. In that roll angle range, Test #3 and Test #2 produced the same mean peak pressure level, while Test #4 resulted in a 1.9 dB increase compared to that value. More precisely, the first three tests provided the same mean value for both peak pressure and duration. An increase was observed for the last two tests (+1.9 dB for Test #4 and +0.9 dB for Test #5). Whereas, the largest standard deviation was measured for Test #3.
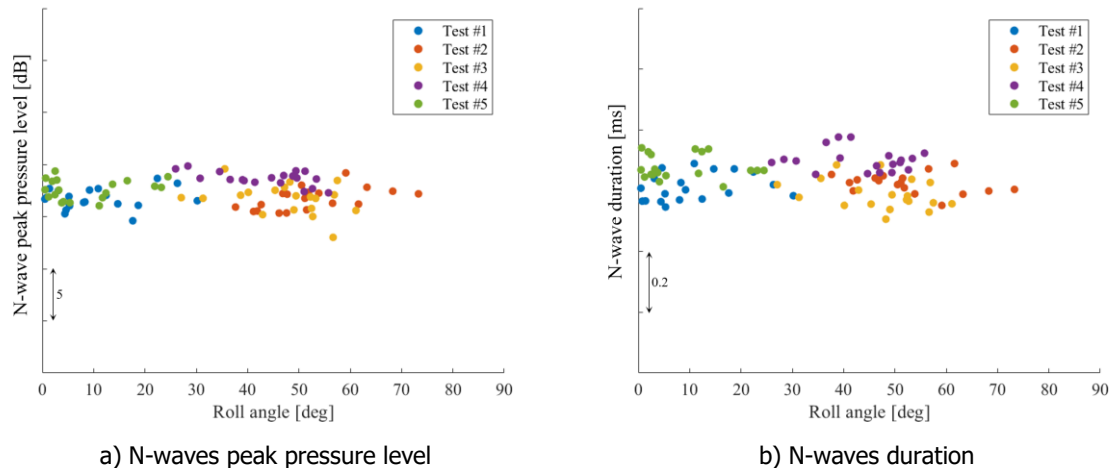

a) N-waves peak pressure level   b) N-waves duration

Fig 25. Corrected N-waves obtained from the 19 ground microphones and grouped by test

In order to explain these observations, the videos of the experiments were analyzed. In the first part of the first test, there is no rotation (up to 30 ms after the launch). Then the model starts to rotate slowly with a constant roll rate. Test #2 exhibits a dynamic characterized by a fairly constant rate of rotation throughout the entire trajectory. Instead, during Test #3, the projectile rapidly rotates to a 90-degree roll angle in less than 20 milliseconds. It then slows down and maintains a nearly constant rotational speed for 75 milliseconds. In contrast, the model in Test #4 experiences an initial high-speed roll, longer than Test #3 (about 110 degrees in 60 milliseconds). It then decelerates and proceeds at an almost fixed roll angle. Finally, Test #5 is quite similar to Test #4, except that the resulting rotational speed is lower (about 80 degrees in 60 milliseconds).

The analysis suggests that the shock wave measurements may have been affected by various factors, such as the projectile's rapid angular acceleration, the high rotational speed, and the inability to maintain a constant rotational speed in the acoustic measurement zone. Indeed, the procedure for estimating the projectile roll angle assumes a constant rotational speed from the entrance frame to the exit frame. Although this approximation is acceptable for Test #1 and Test #2, it may not be accurate for Test #3 to Test #5. Consequently, there is a risk that the measured peak pressures and durations may not be precisely associated with the effective roll angles.

5. Conclusions

As part of the MOREandLESS project, an outdoor sonic boom test campaign was carried out at the ISL test ground in Saint-Louis, France. The experimental activity was conducted over two days, October 4 and 5, on a reduced and slightly modified version of the STRATOFLY MR3 vehicle, launched from a 91 mm smooth-bore powder cannon at an initial Mach number of 4.7. Measurements of the sonic boom were carried out at various points along the range by means of metrological condenser pressure and free field microphones deployed on the ground by ISL and CIRA. To obtain a comprehensive and efficient characterization of sonic boom across the entire roll angle range, ISL also provided three microdrones equipped with microphones and data recorders, which were set in stationary flight, vertically to the firing line, at varying heights.

The recorded signals were gathered and post-processed to assess the combined effect of roll motion (which is not imposed, but is the result of manufacturing model uncertainties and different initial positions) and the model's non-axisymmetry on the measured overpressure signatures. The resulting

noise directivity pattern revealed a common tendency for both ISL and CIRA results: the peak pressure of the N-waves increases with roll angle, while the time duration of the N-waves decreases. It is worth noting that the N-wave peak pressure levels measured in some tests deviated more from the expected trend or had a larger standard deviation. Based on the analysis of the experiment videos, it appears that the shock wave measurements may have been influenced by several factors, including the projectile's rapid angular acceleration, the high rotational speed, and the inability to maintain a constant rotational speed in the acoustic measurement zone (inaccurate estimation of roll angles).

Furthermore, the comparison of Whitham's modified linear theory predictions with experimental acoustic data indicated that the method used, despite its limitations (normal area distribution assumption and intrinsic limitation of Whitham's formulation for hypersonic regime), was capable of predicting the essential characteristics (mean behavior) of the sonic boom generated by the modified STRATOFLY MR3 scaled model. These results are in agreement with NASA experiments, where the Whitham theory provides accurate predictions even for high Mach numbers when the contribution of lift to sonic boom is much smaller than the contribution due to volume (very low lift coefficient). Specifically, in the case study, Whitham's modified linear theory produced reliable results with a mean absolute error for peak pressure level of 1.5 dB with and a standard deviation of 0.6 dB, and a mean error of 0.018 ms with a 0.017 ms standard deviation for the N-wave duration estimation.

The data presented in this paper will be used to experimentally validate numerical scaled models developed in the same project. Furthermore, some effort will also be devoted in using the gathered data to estimate ground N-waves generated by the corresponding full-scale aircraft.

References

1. O'Neill, S.: Supersonic Travel Seeks an Encore. Eng. (2022). https://doi.org/10.1016/j.eng.2022.01.004

2. Richwine, D.: X-59 Aircraft Overview and Status. In AIAA SciTech Forum (2023)

3. Hardeman, A.; Maurice, L. Sustainability: Key to enable next generation supersonic passenger flight. IOP Conf. Ser. Mater. Sci. Eng. (2021). https://doi.org/10.1088/1757-899X/1024/1/012053

4. RUMBLE-RegUlation and norM for Low Sonic Boom LEvels. https://cordis.europa.eu/project/id/769896 (2017). Accessed 1 January 2024

5. Piccirillo, G., Viola, N., Fusaro, R., & Federico, L.: Guidelines for the LTO Noise Assessment of Future Civil Supersonic Aircraft in Conceptual Design. Aero. (2022). https://doi.org/10.3390/aerospace9010027

6. ICAO: Destination Green: The Next Chapter. In Environmental Report (2019)

7. Steelant, J.: ATLLAS: Aero-thermal loaded material investigations for high-speed vehicles. In 15th AIAA International Space Planes and Hypersonic Systems and Technologies Conference. (2008)

8. Steelant, J., Varvill, R., Walton, C., Defoort, S., Hannemann, K., Marini, M.: Achievements obtained for sustained hypersonic flight within the LAPCAT-II project. In 20th AIAA international space planes and hypersonic systems and technologies conference. (2015)

9. Blanvillain, E., Gallic, G.: HIKARI: Paving the way towards high-speed air transport. In 20th AIAA International Space Planes and Hypersonic Systems and Technologies Conference. (2015)

10. Steelant, J., Langener, T., Hannemann, K., Marini, M., Serre, L., Bouchez, M., Falempin, F.: Conceptual design of the high-speed propelled experimental flight test vehicle HEXAFLY. In 20th AIAA international space planes and hypersonic systems and technologies conference. (2015)

11. Steelant, J., Villace, V., Kallenbach, A., Wagner, A., Andro, J. Y., di Benedetto, S., & Buttsworth, D: Flight testing designs in HEXAFLY-INT for high-speed transportation. Proceedings of HiSST. (2018)

12. Viola, N., Fusaro, R.A., Saracoglu, B.H., Schram, C., Grewe, V., Martínez, J.A., Marini, M., Hernández, S., Lammers, K., Vincent, A., Hauglustaine, D., Liebhardt, B., Linke, F., & Fureby, C.: Main challenges and goals of the H2020 STRATOFLY project. Aerotec. Missili Spaz. (2021). https://doi.org/10.1007/s42496-021-00082-6

13. Project-MORE&LESS. https://cordis.europa.eu/project/id/101006856 (2020). Accessed 1 January 2024.

14. Maglieri, D. J., Bobbitt, P. J., Plotkin, K. J., Shepherd, K. P., Coen, P. G., Richwine, D. M.: Sonic boom: Six decades of research. (2014)

15. Loubeau, A., Page, J.: Human perception of sonic booms from supersonic aircraft. Acoust. Today, 14(3), 23-30 (2018)

16. Rylander, R., Sörensen, S., Berglund, K., Brodin, C.: Experiments on the Effect of Sonic-Boom Exposure on Humans. The Journal of the Acoustical Society of America, 51(2C), 790-798 (1972)

17. Rylander, R., Sörensen, S., Andrae, B. O., Chatelier, G., Espmark, Y., Larsson, T., Thackray, R. I.: Sonic boom exposure effects—A field study on humans and animals. Journal of Sound and Vibration, 33(4), 471-IN6 (1974)

18. Ordaz, I., Wintzer, M., Rallabhandi, S. K.: Full-carpet design of a low-boom demonstrator concept. In 33rd AIAA Applied Aerodynamics Conference. (2015)

19. Ritzel, D. V., Gottlieb, J. J.: The overpressure signature from a supersonic projectile. UTIAS Report, No. 279 (1987)

20. Whitham, G. B: The flow pattern of a supersonic projectile. Communications on pure and applied mathematics, 5(3), 301-348 (1952)

21. Walkden, F.: The shock pattern of a wing-body combination, far from the flight path. Aeronautical quarterly, 9(2), 164-194 (1958)

22. Steward, B. J., Gross, K. C., & Perram, G. P.: Characterization and discrimination of large caliber gun blast and flash signatures. In Airborne Intelligence, Surveillance, Reconnaissance Systems and Applications IX. (2012)

23. Carlson, H. W., Mack, R. J.: A wind-tunnel study of the applicability of far-field sonic-boom theory to the space shuttle orbiter. (1978)

24. Carlson, Harry W. Simplified sonic-boom prediction. (1978)

25. Miller, D. S., Carlson, H. W., Morris, O. A.: Wind-tunnel investigation of sonic-boom characteristics of two simple wing models at Mach numbers from 2.3 to 4.63. (1971)

26. Schwartz, I. R. (Ed.).: Third conference on sonic boom research. Scientific and Technical Information Office, National Aeronautics and Space Administration. (1971)